Remote Sensing Applications: Society and Environment 26 (2022) 100763

Contents lists available at ScienceDirect

Remote Sensing Applications: Society and Environment

journal homepage: www.elsevier.com/locate/rsase

Coastal landform changes on the east coast of Sri Lanka using remote sensing and geographic information system (GIS) techniques

W.A.D.B. Weerasingha, Amila Sandaruwan Ratnayake *

Department of Applied Earth Sciences, Faculty of Applied Sciences, Uva Wellassa University, Passara Road, Badulla, 90000, Sri Lanka

ARTICLE INFO

Keywords:
Shoreline change
Coastal erosion
Coastal accretion
Landsat
Digital shoreline analysis system

ABSTRACT

Coastal landforms are constantly changed due to both natural and anthropogenic forces. An attempt is made to analyze short-term coastal landform changes on the east coast of Sri Lanka using remote sensing and geographic information system (GIS) techniques. Such landform changes can be classified as either negative (e.g. erosion) or positive (e.g. accretion) impacts. Surface reflectance images of Landsat 5 Thematic Mapper (TM), Landsat 7 Enhanced Thematic Mapper Plus (ETM+), and Landsat 8 Operational Land Imager/Thermal Infrared Sensor (OLI/TIRS) were analyzed for extracting spatial and temporal changes, based on cross-shore profile analysis and geomorphic change detection. In this study, we developed a novel script model built-in ArcMap for image pre-processing and processing. This model covers six functioning areas of mosaic, land feature extraction, cloud layer generation, vectorization, cloud masking, and smoothing. The green band and mid-infrared images were selected due to the largest reflectance difference between water and non-water bodies. These images have proceeded with modified normalized difference water index (i.e. algorithm of the script model for extracting water and land features). We also quantified the landform changes such as net shoreline movement, shoreline change envelope, endpoint rate, and linear regression rate, using a digital shoreline analysis system (i.e. statistical software combined with ArcMap™). Therefore, landform changes were classified as erosion (>−2.5 m/year), minor seasonal changes (−2.5 m/year to +2.5 m/year), accretion (>+2.5 m/year), based on the annual variations of endpoint rate (i.e. the distance between the oldest and the youngest shorelines to particular time interval). We visualized spatial and temporal coastal landform changes along the east of Sri Lanka, and also identified short-term landform change drives such as tsunamis, cyclones, and anthropogenic activities (e.g. engineering constructions). These landform changes were observed with a global positioning system (GPS)-based field survey. The understanding of such impacts can be directly applied to sustainable coastal zone management.

1. Introduction

Shoreline changes are dependent on several factors such as regular oceanic waves from monsoon winds, longshore currents, rise in sea level, short-term natural processes (e.g. tsunami, typhoon), and anthropogenic activities (Palamakumbure et al., 2020; Gunasinghe

* Corresponding author.
E-mail address: as_ratnayake@uwu.ac.lk (A.S. Ratnayake).

https://doi.org/10.1016/j.rsase.2022.100763
Received 13 February 2022; Received in revised form 11 April 2022; Accepted 17 April 2022
Available online 20 April 2022

et al., 2021). These geomorphological changes can be categorized as positive (coastal accretion) and negative (coastal erosion) impacts on the stability of the coastal sediment budget (Desprats et al., 2010; Ratnayake et al., 2019; Quang et al., 2021). The identification of local/regional coastal erosion can be recognized as an initiative for any coastal zone management action. Dynamic changes in coastal areas can be explored mainly using two methods of remote sensing and beach surveying (Thomas et al., 2020; Islam et al., 2020; Ratnayakage et al., 2020). Previous investigations have analyzed geomorphological changes in the nearshore areas using several remote sensing methods with different precision and accuracy levels (Desprats et al., 2010; Ratnayake et al., 2018; Duong et al., 2021). These remote sensing methods have been widely used due to many advantages such as the ability (i) to collect information over large spatial areas, (ii) to characterize natural features or physical objects on the ground, (iii) to observe the surface area and objects on a

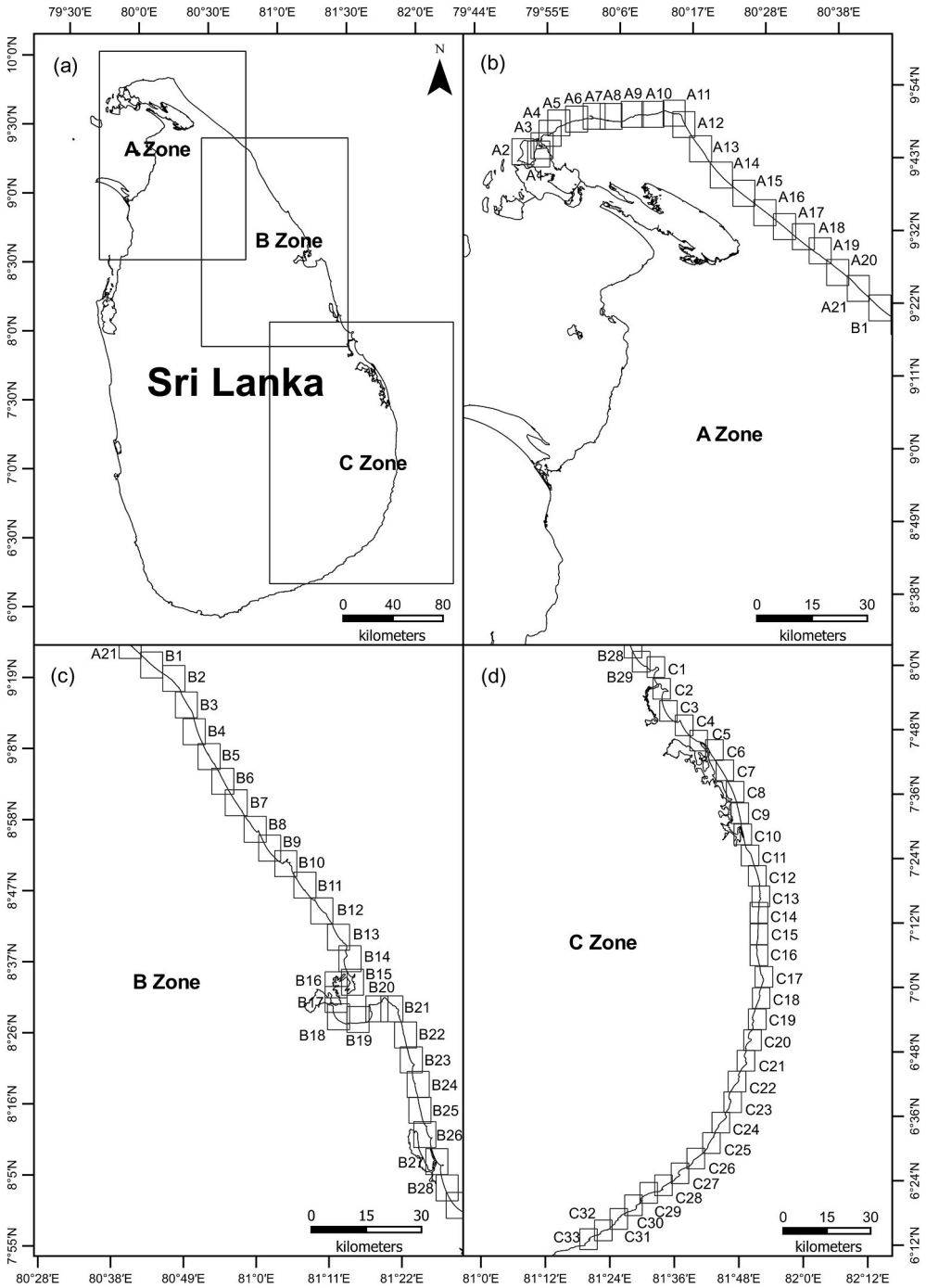

Fig. 1. Major geographical zones of the east coast and its subsets.

systematic basis and monitor their changes over time, and (iv) to integrate satellite data with other information to aid decision making.

Sri Lanka has a coastline spanning over 2000 km in length inclusive of geomorphological features such as lagoons, bays, and islets (Lowry and Wickremeratne, 1988). Several case studies have been carried out to determine quantitative and qualitative coastal erosion mainly along the south and west coasts of Sri Lanka (Amalan et al., 2018; Senevirathna et al., 2018; Duong et al., 2021). However, only a very few studies have focused to identify such coastal changes along the east coast of Sri Lanka. The east coast of Sri Lanka consists of several harbors (e.g. Hambantota, Oluvil, Trincomalee), urbanization areas/tourist hotspots (e.g. Arugambay, Pasikuda, Nilaveli), and archeological and biological conservation sites (e.g. Kumana and Yala national parks), and high-grade mineral deposits (e.g. Verugal, Pulmoddai, Kokkilai) (Adikaram et al., 2021; Subasinghe et al., 2021). Therefore, the eastern coastal belt of Sri Lanka is an environmental hotspot and an important zone for the country's development. Besides, the east coast of Sri Lanka experienced rapid urbanization, and implemented several development projects after the end of the civil war in 2009. Consequently, the objective of this study is to quantify the shoreline changes and examine sediment dynamics over the last two decades. In this paper, we analyzed detailed morphological changes along the east coast of Sri Lanka covering 600 km based on Landsat digital maps.

2. Methodology

This study covers the entire eastern coastal area from Karainagar to Bundala (Fig. 1). The study area was divided into three major geographical zones (labeled as A, B, and C). These major geographical zones were further divided into subsets, A ($n = 21$), B ($n = 29$), and C ($n = 33$), with each an area of 43 km^2 (Fig. 1).

The United States Geological Survey (USGS) provides surface reflectance data of Landsat 5 Thematic Mapper (TM), Landsat 7

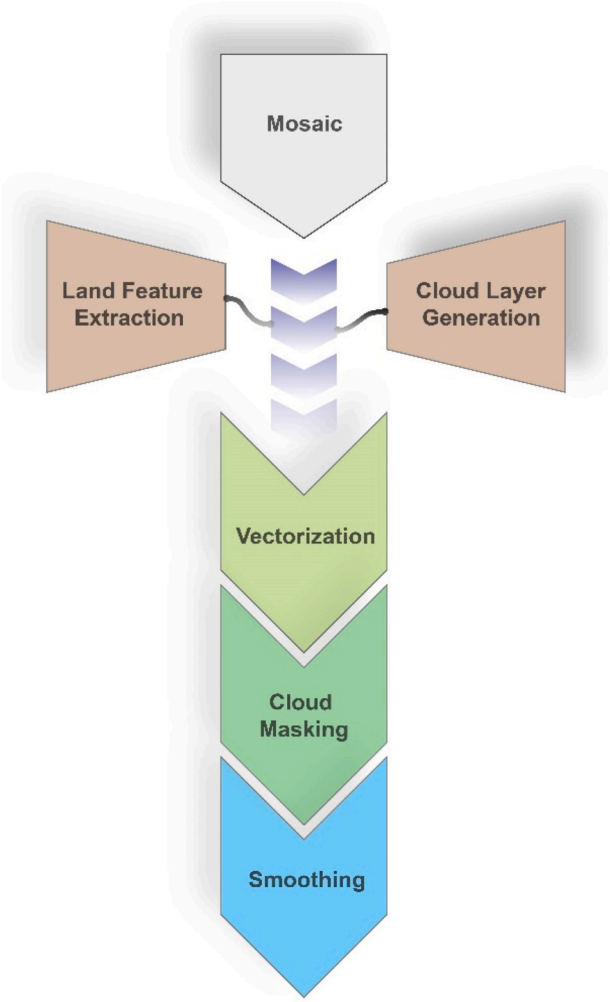

Fig. 2. The main steps of the script model.

$$MNDWI = (band_{Green} - band_{SWIR2})/(band_{Green} + band_{SWIR2}) \quad \text{(Eq 1)}$$

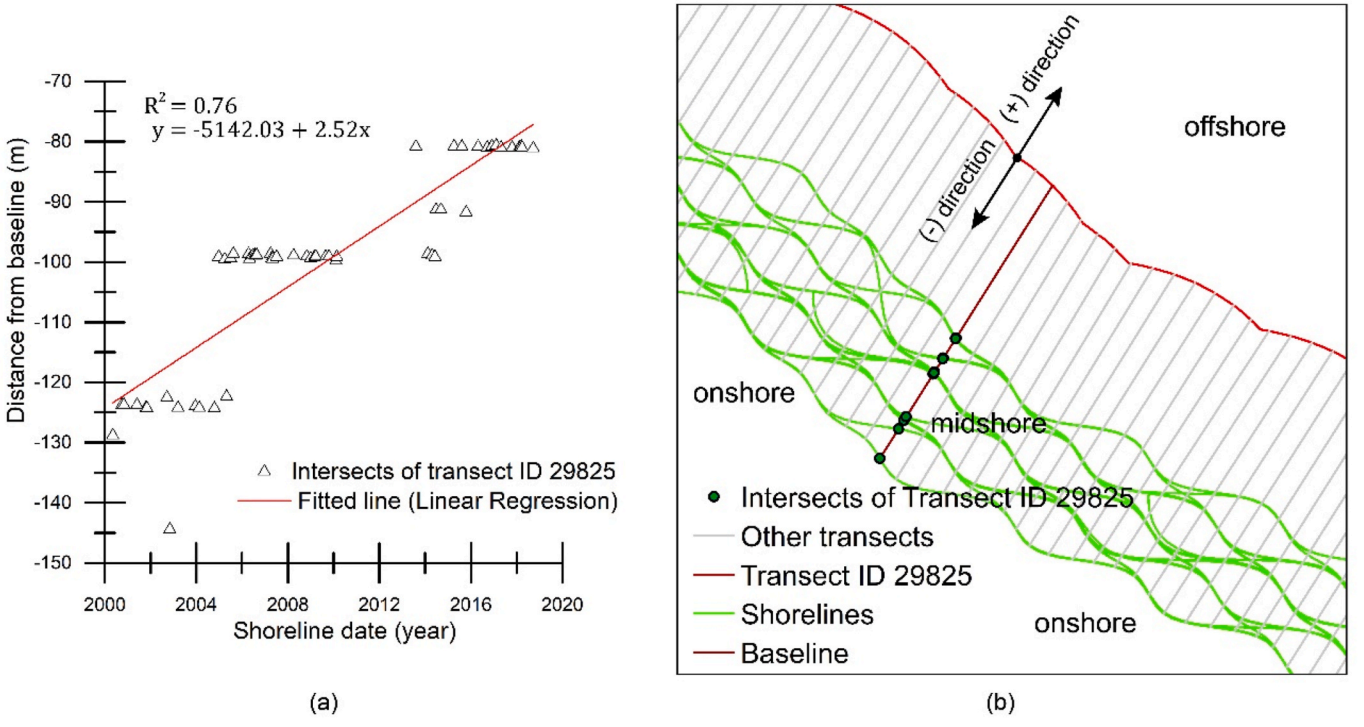

Fig. 3. Demonstration of linear regression rate, (a) chart of linear regression and, (b) shoreline, baseline, and transect ID 29825 (which includes in C5 subset), as an example.

Enhanced Thematic Mapper Plus (ETM+), and Landsat 8 Operational Land Imager/Thermal Infrared Sensor (OLI/TIRS) through Earth Explorer, which have 30 m spatial resolution. Scene cloud and land cloud covers are included in Landsat level-1 data. The C Function of Mask (CFMask) algorithm calculates the percentage of cloud cover over an entire Landsat scene (Foga et al., 2017). Land cloud cover was utilized to calculate the percentage of clouds. In this step, the world vector shoreline dataset of the National Oceanic and Atmospheric Administration (NOAA) was used to distinguish land from water interfaces. Less than 50 percent of land cloud covers were selected for generating level-2 data (i.e. for extracting undisturbed shorelines).

Top-of-atmospheric reflectance values depend on the nature of the earth's surface and atmospheric aerosols/gases conditions. Landsat surface reflectance is defined as the fraction of solar radiation that reaches the Landsat sensor after being reflected from the earth's surface. In this case, surface reflectance is derived from top-of-atmospheric values. Therefore, surface reflectance helps to characterize the earth's surface change (Vermote et al., 2016). The Earth Resources Observation and Science Center of the USGS corrects satellite images for atmospheric effects using Landsat ecosystem disturbance adaptive processing system (LEDAPS) software for Landsat 5 and 7 data (Masek et al., 2006). The land surface reflectance (LaSRC) code is used for Landsat 8 data (Vermote et al., 2016). These generated surface reflectance images are known as level-2 data.

In this study, path/row numbers of 142/053, 141/053, 141/054, 140/055 and 140/056 in the worldwide reference system (WRS–2) were selected to obtain Landsat data covering the east coast of Sri Lanka (See appendix 1). Image pre-processing and processing were carried out using a model builder in ArcMap. This model consists of six functioning zones of mosaic, land feature extraction, cloud layer generation, vectorization, cloud masking, and smoothing (Fig. 2 and Appendix 2). The green band (0.519–0.601 μm), shortwave infrared (SWIR 2) band (2.064–2.345 μm) and cloud band (sr_aerosoal: belongs to Landsat 8 and sr_cloud_qa: belong to Landsat 5 and 7) of collection 1 tier 1 level-2 data products were fed on the script model (Asmadin et al., 2018). Data products of level-2 were merged band-wise using mosaic processes. The mosaic images of the green band and mid-infrared band have proceeded with the modified normalized difference water index (MNDWI) value (Xu, 2006). Shoreline extraction and mapping were performed based on the calculated MNDWI threshold value for Landsat data.

The optimum threshold value was decided by several reclassification tests with QuickBird images. The MNDWI values range from −1 to +1, and can be used to separate land features from water features. These land and water interfaces were reclassified to two different binary values (Acharya et al., 2018). The final output is vectorized, and smoothed polylines are identified as shorelines. The shoreline accuracy assessment was done with reference shoreline extracted from Google Earth images (See Appendix 3 for the accuracy assessment of the model).

The digital shoreline analysis system (DSAS) was used to calculate spatial and temporal shoreline movements (Himmelstoss et al., 2018; Quang et al., 2021). The software is based on three major parts of baseline, shorelines, and transects. The baseline was constructed using the buffering process. All selected shorelines were merged into one feature class and created a buffer zone. The transects were generated perpendicular to the reference baseline with 10 m spacing. The outputs of the script model have proceeded to DSAS for analysis of coastal changes. The net shoreline movement, shoreline change envelope, endpoint rate, and linear regression rate were calculated using the DSAS. Field observations were used to validate model results.

The net shoreline movement (NSM) is the distance between the oldest and the youngest shorelines for each transect.

$$NSM = (oldest\ shoreline_{distance} - youngest\ shoreline_{distance}) \quad \text{(Eq.2)}$$

The shoreline change envelope (SCE) is the greatest distance among all the shorelines for a given transect. The value for SCE is always positive.

$$SCE_{relative\ to\ baseline} = (farthest\ shoreline_{distance} - nearest\ shoreline_{distance}) \quad \text{(Eq 3)}$$

The endpoint rate (EPR) is calculated by dividing the distance between the oldest and the youngest shorelines into a particular time interval.

$$EPR = \frac{(net\ shoreline\ movement_{distance})}{(time\ between\ oldest\ and\ young\ shoreline)} \quad \text{(Eq 4)}$$

The linear regression rate (LRR) can be determined by fitting a least-squares regression line to all shoreline points for a transect (Fig. 3). This method calculates the best-fitting line for all observed data. The deviations were first squared, and then summed. There are no cancellations between positive and negative values. The explanatory variable (x) is the shoreline date in years, and the dependent variable (y) is the distance from baseline in meters. Therefore, the linear regression rate is the slope of the line (Himmelstoss et al., 2018). (See Fig. 3 for identifying how to plot a linear regression line using intersects of transect ID 29825).

$$LRR = \frac{(\delta y - c)}{\delta x} \quad \text{(Eq 5)}$$

3. Results and discussion

3.1. Shoreline change rates

The net shoreline movement, shoreline change envelope, endpoint rate, and linear regression rate values in major geographical zones of A, B and C are shown in Tables 1–3, respectively. These results indicate coastal erosional and accretion for each subset during the last 18 years. The selected visualization results of endpoint rate in major geographical zones of A, B and C are shown in Figs. 4–6, respectively. In this study, endpoint rates were classified into three classes based on the annual variations, such as erosion (>–2.5 m/

year), minor seasonal changes (−2.5 m/year to +2.5 m/year), accretion (>+2.5 m/year) (See Appendix 3 for the accuracy assessment). The maximum erosions in major geographical zones of A, B, and C are recorded in subsets of A1 (endpoint rate = −59.71 m/year), B20 (endpoint rate = −12.67 m/year), and C1 (endpoint rate = −20.90 m/year), respectively (Tables 1–3). In contrast, maximum accretion in major geographical zones of A, B, and C are recorded in subsets of A3 (endpoint rate = +36.92 m/year), B27 (endpoint rate = +31.17 m/year), and C5 (endpoint rate = +31.30 m/year), respectively (Tables 1–3).

The values of endpoint rate, linear regression rate, shoreline change envelope, and net shoreline movement were also plotted with the transects for identifying erosional or accretion anomalies (Figs. 7–9). Besides, selected QuickBird satellite images from Google Earth show such erosional or accretion anomalies of the study area (Fig. 10). The net shoreline movement values in Fig. 10 were also classified into three classes, such as erosion (>–2.5 m), minor coastal changes (−2.5 m to +2.5 m), and accretion (>+2.5 m).

3.2. Observations

3.2.1. Study zone A

Study zone A consists of Karainagar Island and the Jaffna Peninsula. Karainagar Island and Ponnali Khadu urban areas are affected by remarkable shoreline changes since 2000 (Fig. 4b). For example, the west part of Karainagar Island shows massive coastal erosion (Figs. 4b and 7a), which may be due to prominent longshore currents in a shallow marine continental shelf (Ratnayake, 2016). In addition, the Kovalam and Casuarina beaches are accreted by eroded sediment probably from Karainagar Island (Figs. 4a and 7b). Consequently, temporal coastal erosion suggests counterclockwise sediment transportation in Karainagar Island and the Jaffna Peninsula. In contrast, both accretion (around Valalai and Palaly areas in Fig. 4c and Palmyra Point beach, Point Pedro areas in Fig. 4d) and erosion (Moorkam beach in Fig. 4d) are visible in study zone A. In general, this study zone can be recognized as an area for sand

Table 1
Statistics of net shoreline movement (NSM), shoreline change envelope (SCE), endpoint rate (EPR), and linear regression rate (LRR) in A zone, based on a digital shoreline analysis system.

Subset	Max/Min	NSM (m)		EPR (m/year)		LRR (m/year)		SCE (m)
		Erosion	Accretion	Erosion	Accretion	Erosion	Accretion	
A01	Max	−1058	88.85	−59.71	4.82	−31.88	5.53	1244.34
	Min	−0.01	0.01	−0.01	0.01	−0.01	0.01	8.94
A02	Max	−50.36	110.35	−2.73	5.98	−1.72	6.71	208.99
	Min	−0.01	0.01	−0.01	0.01	−0.01	0.01	0.37
A03	Max	−464.14	552.22	−26.20	36.92	−11.00	29.44	553.27
	Min	−0.01	0.01	−0.01	0.01	−0.01	0.01	19.81
A04	Max	−30.61	365.05	−1.72	20.06	−5.68	6.11	796.39
	Min	−0.01	0.01	−0.01	0.01	−0.01	0.01	16.62
A05	Max	−30.61	31.88	−1.72	1.71	−0.80	3.58	410.24
	Min	−0.01	0.01	−0.01	0.01	−0.01	0.01	18.48
A06	Max	−30.74	29.50	−1.73	1.68	−0.82	2.06	241.09
	Min	−0.01	0.01	−0.01	0.01	−0.01	0.01	0.83
A07	Max	−81.93	176.91	−4.61	11.35	−5.39	10.23	177.08
	Min	−0.01	0.01	−0.01	0.01	−0.01	0.01	0.06
A08	Max	−199.17	89.51	−10.79	5.04	−4.41	4.25	232.41
	Min	−0.01	0.01	−0.01	0.01	−0.01	0.01	5.85
A09	Max	−30.31	95.77	−1.69	5.34	−5.67	7.80	366.95
	Min	−0.01	0.01	−0.01	0.01	−0.01	0.01	5.64
A10	Max	−30.70	60.93	−1.73	3.27	−0.99	2.49	140.05
	Min	−0.01	0.01	−0.01	0.01	−0.01	0.01	5.30
A11	Max	−58.9	63.12	−3.28	3.39	−2.68	2.23	130.27
	Min	−0.01	0.01	−0.01	0.01	−0.01	0.01	5.41
A12	Max	−58.9	32.98	−3.28	1.77	−2.78	1.41	304.92
	Min	−0.01	0.01	−0.01	0.01	−0.01	0.01	18.36
A13	Max	−33.09	53.00	−1.87	2.84	−1.13	1.84	242.07
	Min	−0.01	0.01	−0.01	0.01	−0.01	0.01	18.07
A14	Max	−0.62	34.43	−0.03	1.87	−0.36	1.03	67.18
	Min	−0.01	0.02	−0.01	0.01	−0.01	0.01	17.82
A15	Max	−0.6	44.45	−0.03	2.38	−0.74	0.57	64.96
	Min	−0.04	0.02	−0.01	0.01	−0.01	0.01	17.99
A16	Max	−0.62	44.27	−0.03	2.38	−0.67	0.54	130.13
	Min	−0.03	0.04	−0.01	0.01	−0.01	0.01	18.30
A17	Max	−0.59	43.73	−0.03	2.35	−0.54	0.58	73.68
	Min	−0.01	0.05	−0.01	0.01	−0.01	0.01	18.4
A18	Max	−0.61	43.61	−0.03	2.34	−1.08	0.46	70.24
	Min	−0.01	0.01	−0.01	0.01	−0.01	0.01	18.62
A19	Max	−33.15	406.67	−1.78	21.82	−7.44	5.69	502.39
	Min	−0.01	0.01	−0.01	0.01	−0.01	0.01	18.11
A20	Max	−0.55	406.67	−0.03	21.82	−1.11	5.69	424.76
	Min	−0.04	0.13	−0.01	0.01	−0.01	0.01	18.26
A21	Max	−22.59	103.34	−1.21	5.54	−1.11	1.08	157.88
	Min	−0.01	0.01	−0.01	0.01	−0.01	0.01	18.25

Table 2
Statistics of net shoreline movement (NSM), shoreline change envelope (SCE), endpoint rate (EPR), and linear regression rate (LRR) in B zone, based on a digital shoreline analysis system.

Subset	Max/Min	NSM (m)		EPR (m/y)		LRR (m/y)		SCE (m)
		Erosion	Accretion	Erosion	Accretion	Erosion	Accretion	
B01	Max	−24.98	34.94	−1.34	1.87	−0.55	1.22	70.06
	Min	−0.03	0.05	−0.01	0.01	−0.01	0.01	17.88
B02	Max	−61.29	108.25	−3.29	5.81	−4.90	5.78	484.39
	Min	−0.01	0.01	−0.01	0.01	−0.01	0.01	18.39
B03	Max	−61.29	60.67	−3.29	3.25	−3.13	2.00	103.36
	Min	−0.01	0.01	−0.01	0.01	−0.01	0.01	19.62
B04	Max	−31.88	32.91	−1.73	1.79	−1.30	1.07	90.32
	Min	−0.01	0.01	−0.01	0.01	−0.01	0.01	5.81
B05	Max	−0.62	34.43	−0.03	1.87	−0.36	1.03	67.18
	Min	−0.01	0.02	−0.01	0.01	−0.01	0.01	17.82
B06	Max	−73.73	130.43	−4.00	7.08	−2.04	1.15	457.94
	Min	−0.01	0.01	−0.01	0.01	−0.01	0.01	19.67
B07	Max	−63.07	46.8	−3.42	2.54	−1.68	0.70	75.14
	Min	−0.01	0.01	−0.01	0.01	−0.01	0.01	9.50
B08	Max	−105.32	214.02	−5.76	11.48	−3.88	2.70	599.09
	Min	−0.01	0.01	−0.01	0.01	−0.01	0.01	18.96
B09	Max	−43.74	188.39	−2.35	10.11	−2.08	8.85	518.08
	Min	−0.01	0.01	−0.01	0.01	−0.01	0.01	19.37
B10	Max	−23.45	188.39	−1.26	10.11	−2.08	8.85	518.08
	Min	−0.02	0.01	−0.01	0.01	−0.01	0.01	18.66
B11	Max	−35.29	60.79	−1.89	3.26	−1.70	2.19	301.75
	Min	−0.01	0.01	−0.01	0.01	−0.01	0.01	5.73
B12	Max	−24.03	100.54	−1.29	5.39	−1.18	3.27	675.63
	Min	−0.01	0.01	−0.01	0.01	−0.01	0.01	17.98
B13	Max	−218.74	375.56	−11.74	20.15	−9.35	11.85	398.06
	Min	−0.01	0.01	−0.01	0.01	−0.01	0.01	18.12
B14	Max	−25.57	47.11	−1.37	2.53	−1.12	1.62	231.38
	Min	−0.01	0.01	−0.01	0.01	−0.01	0.01	18.83
B15	Max	−96.94	135.19	−5.20	7.25	−3.45	3.05	272.86
	Min	−0.01	0.01	−0.01	0.01	−0.01	0.01	0.62
B16	Max	−100.92	555.74	−5.41	29.82	−2.28	19.10	598.45
	Min	−0.01	0.01	−0.01	0.01	−0.01	0.01	0.56
B17	Max	−76.99	152.99	−4.13	8.21	−1.46	5.34	298.73
	Min	−0.01	0.01	−0.01	0.01	−0.01	0.01	0.56
B18	Max	−34.68	63.71	−1.86	3.42	−1.88	1.62	122.78
	Min	−0.01	0.01	−0.01	0.01	−0.01	0.01	20.66
B19	Max	−64.09	306.43	−3.50	16.44	−9.71	10.76	773.10
	Min	−0.01	0.01	−0.01	0.01	−0.01	0.01	0.62
B20	Max	−236.21	191.66	−12.67	10.41	−18.94	11.95	387.60
	Min	−0.08	0.02	−0.01	0.01	−0.01	0.05	6.78
B21	Max	−63.13	68.30	−3.43	3.66	−3.37	5.86	223.75
	Min	−0.01	0.01	−0.01	0.01	−0.01	0.01	5.47
B22	Max	−65.24	121.28	−3.50	6.51	−2.97	4.73	384.10
	Min	−0.01	0.01	−0.01	0.01	−0.01	0.01	18.33
B23	Max	−62.78	48.81	−3.37	2.62	−2.36	1.66	140.97
	Min	−0.01	0.01	−0.01	0.01	−0.01	0.01	21.73
B24	Max	−44.67	216.12	−2.41	11.82	−1.71	2.50	377.54
	Min	−0.01	0.01	−0.01	0.01	−0.01	0.01	11.31
B25	Max	−44.87	202.28	−2.42	10.93	−1.71	1.88	377.54
	Min	−0.01	0.01	−0.01	0.01	−0.01	0.01	22.52
B26	Max	−48.66	331.22	−2.64	17.77	−2.71	5.68	423.22
	Min	−0.01	0.01	−0.01	0.01	−0.01	0.01	19.02
B27	Max	−50.95	580.88	−2.73	31.17	−3.46	8.67	697.44
	Min	−0.01	0.02	−0.01	0.01	−0.01	0.01	30.66
B28	Max	−23.69	46.46	−1.27	2.49	−0.43	1.05	225.46
	Min	−0.01	0.04	−0.01	0.01	−0.01	0.01	19.52
B29	Max	−87.00	101.84	−4.67	5.46	−6.48	2.31	207.39
	Min	−0.01	0.01	−0.01	0.01	−0.01	0.01	17.99

accretion. Furthermore, visualization maps (Figs. 4a and 7b) and a digital shoreline analysis system (Table 1) suggest that nearshore sediments transport mainly from a subset of A21 to A3 (i.e. counterclockwise movement).

3.2.2. Study zone B

Study zone B (Fig. 5) covered several lagoons (e.g. Kokkilai, Sinnakarachchi, Ullackalie, Uppar) and bays (e.g. Dutch, Manayaweli, Koddiyar, Trincomalee). Most of the bay and lagoons in zone B were affected by accretion, but few locations such as Kokkilai Barmouth

Table 3
Statistics of net shoreline movement (NSM), shoreline change envelope (SCE), endpoint rate (EPR), and linear regression rate (LRR) in C zone, based on a digital shoreline analysis system.

Subset	Max/Min	NSM (m)		EPR (m/y)		LRR (m/y)		SCE (m)
		Erosion	Accretion	Erosion	Accretion	Erosion	Accretion	
C01	Max	−384.1	328.86	−20.9	17.9	−45.38	23.35	1063.48
	Min	−0.01	0.02	−0.01	0.01	−0.01	0.01	6.04
C02	Max	−92.43	65.31	−5.03	3.55	−2.67	2.06	149.57
	Min	−0.01	0.01	−0.01	0.01	−0.01	0.01	5.58
C03	Max	−23.4	84.03	−1.27	4.57	−0.84	3.52	90.90
	Min	−0.01	0.01	−0.01	0.01	−0.01	0.01	17.77
C04	Max	−172.01	135.82	−9.36	7.39	−7.93	6.15	242.51
	Min	−0.02	0.05	−0.01	0.01	−0.01	0.01	18.02
C05	Max	−53.96	575.2	−2.94	31.30	−6.27	9.66	814.89
	Min	−0.06	0.02	−0.01	0.01	−0.02	0.02	21.04
C06	Max	−23.40	34.35	−1.27	1.87	−1.44	1.56	90.75
	Min	−0.01	0.01	−0.01	0.01	−0.01	0.01	18.23
C07	Max	−24.79	33.55	−1.35	1.83	−0.65	1.97	109.58
	Min	−0.01	0.01	−0.01	0.01	−0.01	0.01	18.58
C08	Max	−30.85	60.57	−1.68	3.30	−1.09	2.56	88.83
	Min	−0.02	0.02	−0.01	0.01	−0.01	0.01	19.88
C09	Max	−59.23	50.69	−3.22	2.76	−1.39	2.05	91.99
	Min	−0.01	0.01	−0.01	0.01	−0.01	0.01	21.73
C10	Max	−51.17	60.83	−2.78	3.31	−1.95	3.14	542.24
	Min	−0.01	0.01	−0.01	0.01	−0.01	0.01	15.96
C11	Max	−66.69	102.71	−3.63	5.59	−1.83	3.80	215.11
	Min	−0.01	0.01	−0.01	0.01	−0.01	0.01	21.57
C12	Max	−120.65	60.91	−6.57	3.31	−6.18	1.56	391.17
	Min	−0.03	0.01	−0.01	0.01	−0.01	0.01	22.12
C13	Max	−330.74	364.97	−18.00	19.86	−14.15	24.80	517.31
	Min	−0.04	0.64	−0.01	0.03	−0.04	0.04	31.13
C14	Max	−0.7	364.97	−0.04	19.86	−4.13	24.80	517.31
	Min	−0.02	0.01	−0.01	0.01	−0.04	0.29	30.56
C15	Max	−0.67	31.07	−0.04	1.69	−1.04	2.56	299.52
	Min	−0.01	0.01	−0.01	0.01	−0.01	0.02	22.22
C16	Max	−91.73	31.28	−4.99	1.70	−2.78	1.17	293.73
	Min	−0.02	0.01	−0.01	0.01	−0.01	0.01	23.54
C17	Max	−65.28	34.22	−3.55	1.86	−1.71	1.01	156.47
	Min	−0.04	0.01	−0.01	0.01	−0.01	0.01	17.76
C18	Max	−65.6	32.12	−3.57	1.75	−2.20	1.28	165.76
	Min	−0.01	0.01	−0.01	0.01	−0.01	0.01	21.61
C19	Max	−60.52	73.00	−3.30	3.98	−1.68	0.93	178.71
	Min	−0.01	0.01	−0.01	0.01	−0.01	0.01	18.53
C20	Max	−60.35	58.99	−3.29	3.22	−3.05	1.87	465.20
	Min	−0.01	0.01	−0.01	0.01	−0.01	0.01	5.80
C21	Max	−60.51	61.91	−3.30	3.38	−6.82	1.47	580.75
	Min	−0.01	0.01	−0.01	0.01	−0.01	0.01	18.71
C22	Max	−50.03	31.26	−2.73	1.71	−1.96	0.95	151.13
	Min	−0.01	0.01	−0.01	0.01	−0.01	0.01	19.39
C23	Max	−54.33	48.02	−2.96	2.59	−2.23	0.91	183.61
	Min	−0.01	0.01	−0.01	0.01	−0.01	0.01	19.44
C24	Max	−61.00	90.05	−3.30	4.87	−1.06	4.15	228.47
	Min	−0.01	0.01	−0.01	0.01	−0.01	0.01	6.49
C25	Max	−87.42	192.53	−4.72	10.48	−0.86	6.67	584.64
	Min	−0.01	0.01	−0.01	0.01	−0.02	0.01	19.14
C26	Max	−33.5	48.94	−1.86	2.65	−1.28	0.81	132.29
	Min	−0.01	0.01	−0.01	0.01	−0.01	0.01	18.33
C27	Max	−71.95	48.49	−4.01	2.63	−0.93	1.60	175.99
	Min	−0.01	0.01	−0.01	0.01	−0.01	0.01	18.03
C28	Max	−90.35	51.41	−5.04	2.78	−1.96	1.24	257.36
	Min	−0.01	0.01	−0.01	0.01	−0.01	0.01	5.95
C29	Max	−67.65	30.38	−3.66	1.65	−1.70	1.02	211.39
	Min	−0.01	0.01	−0.01	0.01	−0.01	0.01	17.90
C30	Max	−70.82	29.71	−3.95	1.66	−1.09	1.17	209.89
	Min	−0.01	0.01	−0.01	0.01	−0.01	0.01	5.65
C31	Max	−91.66	39.18	−4.96	2.27	−1.81	1.44	143.57
	Min	−0.01	0.01	−0.01	0.01	−0.01	0.01	7.06
C32	Max	−91.96	24.05	−5.13	1.33	−2.17	1.10	119.96
	Min	−0.01	0.01	−0.01	0.01	−0.01	0.01	7.06
C33	Max	−274.42	40.53	−14.86	2.20	−10.1	3.79	312.87
	Min	−0.01	0.01	−0.01	0.01	−0.01	0.01	8.57

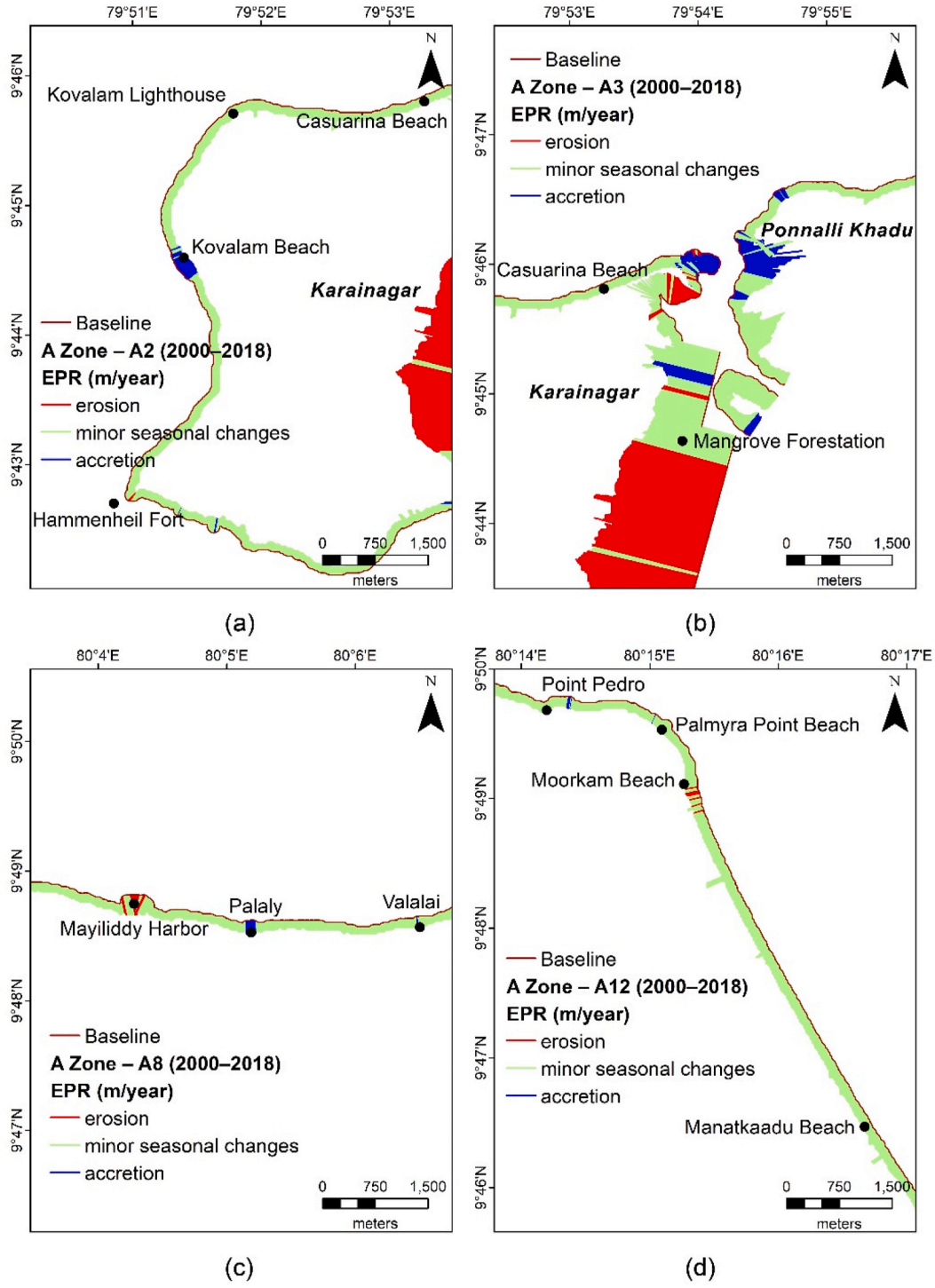

Fig. 4. Visualization results of endpoint rate (EPR) in (a) A2, (b) A3, (c), A8, and (d) A12 subsets.

and Koddiyar Bay were affected by coastal erosion (Fig. 5b, d, and 11d). Similarly, the coastal areas between Karaiyamullivaikkal beach and Nanthi Kadal Lagoon (Fig. 5a), Rathugala (Red Rock) (Fig. 5c), Sinnakarachchi Lagoon outlet (Fig. 5c), Nawarathnapuram (Fig. 5e), Foul Point lighthouse (Fig. 5e), Verugal (Fig. 11), Vaharai and Sallathive (Fig. 5f) areas have been subjected to accretion, whereas the Mullaitivu, Kokkilai black sand beach and Mutur beach have been subjected to erosion (Figs. 5, 8 and 11). In this case, most of the areas in study zone B indicate coastal accretion. Besides, nearshore sediments can probably transport from south to north (counterclockwise movement), according to visualization maps (Figs. 5 and 8) and a digital shoreline analysis system (Table 2).

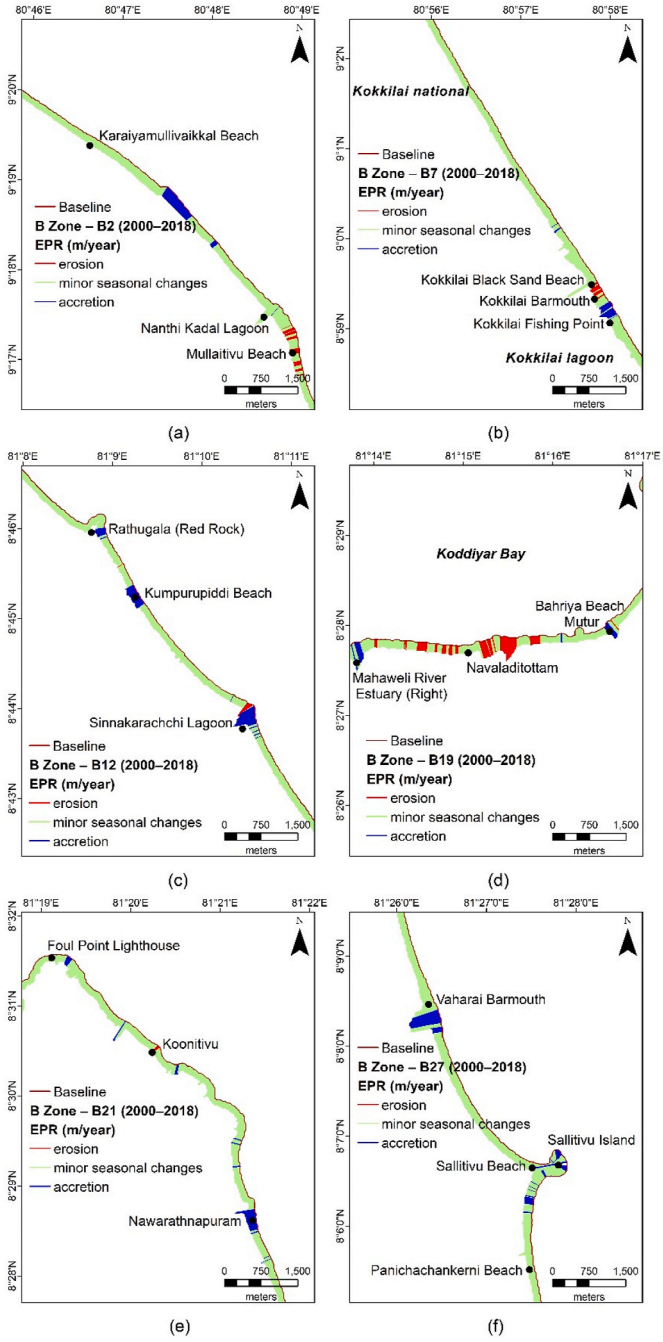

Fig. 5. Visualization results of EPR in (a) B2, (b) B7, (c) B12, (d) B19, (e) B21, and (f) B27 subsets.

3.2.3. Study zone C

Thennadi Bay was affected by coastal erosion, whereas Vandalous Bay was affected by sand accretion (Fig. 6a). It suggests that sediments are predominantly transported from south to north (counterclockwise movement). The Punnakkuda beach (Fig. 6b), and Batticaloa (Figs. 6c and 9a) areas are exposed to coastal accretion. Maruthamunai (Fig. 6e), Thirukkovil (Figs. 6f and 11b), Whisky and Pottuvil (Fig. 6g) beaches are subject to coastal erosion. These observations also suggest sand movement from bottom to top parts in study zone C. However, site-specific observations can also be observed. For example, the estuary of Kumbukkan Oya is subjected to coastal accretion (Fig. 6h), due to a large flux of sediments. In general, visualization maps (Figs. 6 and 9) and a digital shoreline analysis system (Table 3) suggest coastal erosion in the lower part and accretion in the upper part of study zone C.

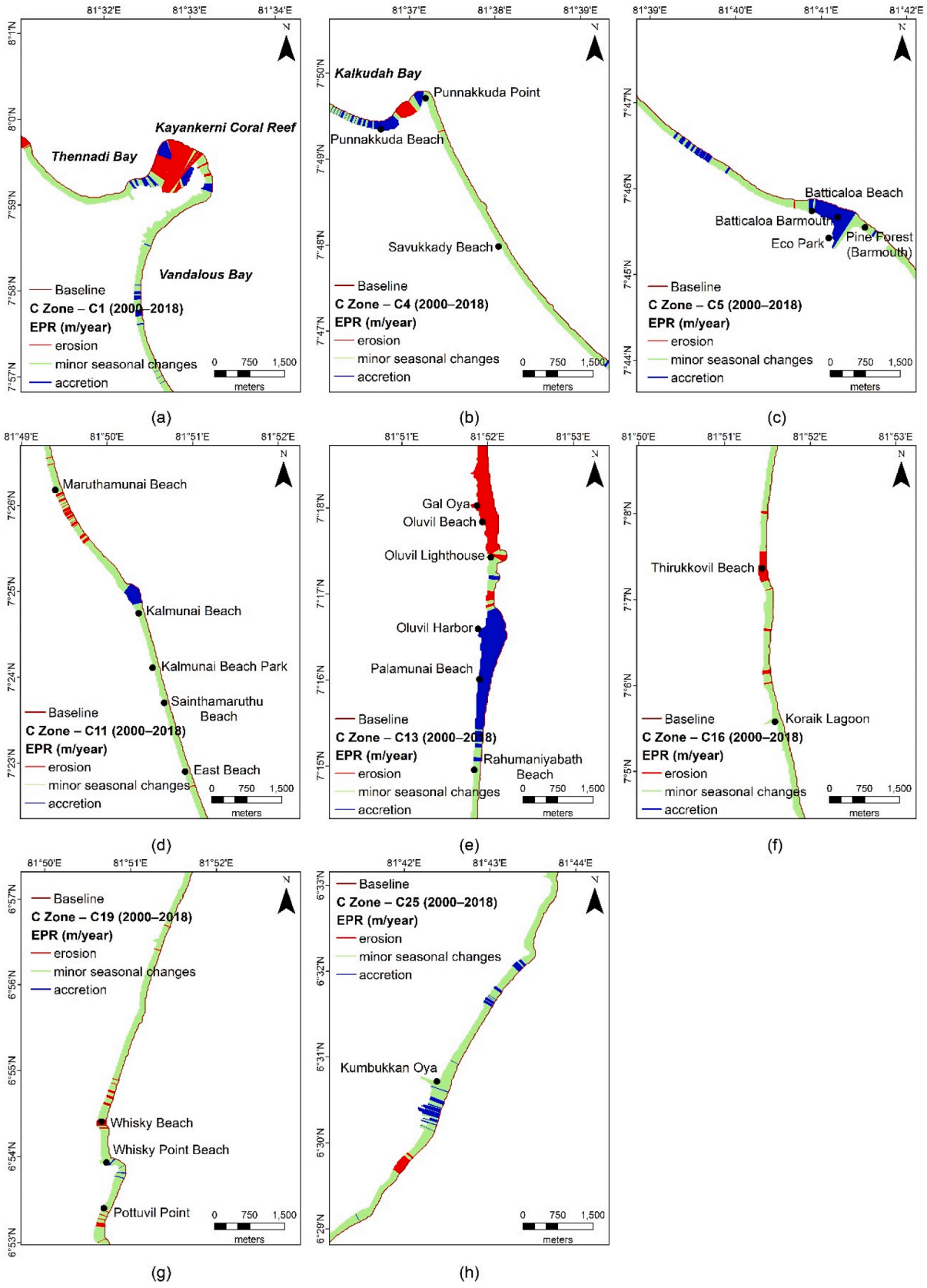

(caption on next page)

Fig. 6. Visualization results of EPR in (a) C1, (b) C4, (c) C5, (d) C11, (e) C13, (f) C16, (g) C19, and (h) C25 subsets.

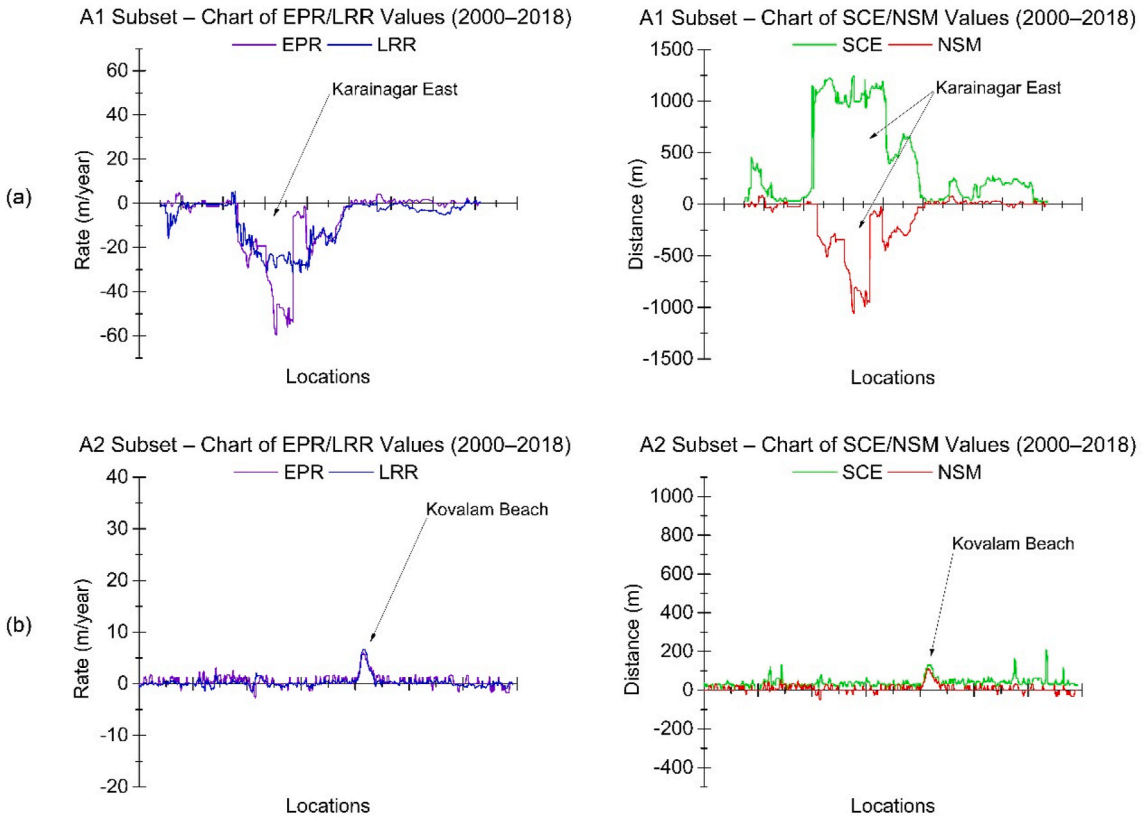

Fig. 7. Digital shoreline analysis system (DSAS) statistical graphs in (a) A1, and (b) A2 subsets.

3.3. Interpretation of dynamic changes

Monitoring and quantifying the rate and distance difference of shoreline changes on the east coast of Sri Lanka are valuable for coastal resources management and conservation. Popular space-borne technologies such as the Landsat program offer powerful multi-temporal satellite data for the exploration of coastal environments and geomorphological changes using the geographic information system (Thomas et al., 2020; Arjasakusuma et al., 2021; Quang et al., 2021). In this study, the model builder in ArcMap is used green band and mid-infrared band data. The mid-infrared band has the largest difference in reflectance values between water and non-water bodies. Therefore, the mid-infrared band exhibits the highest contrast between water and non-water bodies (Malahlela, 2016; Yan et al., 2020). The modified normalized difference water index (MNDWI) algorithm combined with the model can separate land features from oceanic water (Acharya et al., 2016). In addition, we quantified the dynamic changes along the east coast of Sri Lanka using a digital shoreline analysis system (i.e. statistical software combined with ArcMap). Consequently, the digital shoreline analysis system provides qualitative and quantitative results for understanding the coastal sediment budget along this coast.

4. Short-term drivers

Since our study is limited to 18 years, the landform changing factors can be categorized as short-term drives. We discussed here several drives that can trigger landform changes along the east coast of Sri Lanka. The tsunami waves on December 26, 2004 impacted the entire eastern coastline of Sri Lanka. The highest amplitude of tsunami waves was calculated close to the shoreline along the east coast, and it ranged from 2.2 to 11.4 m, with a mean value of 5.7 m. The measured tsunami inundation distance varied from 70 to 4560 m (Wijetunge, 2009). Therefore, the tsunami event in 2004 can be identified as one of the major drivers of short-term landform changes along the east coast of Sri Lanka. Fig. 10a shows that the coastal landforms along the east coast have remarkably altered after the tsunami disaster in 2004. For example, the tsunami waves insight on variations of sediment load due to erosion or deposition (e.g. coastal water bodies filled with debris) processes (Wijeratne, 2016; Satyanarayana et al., 2017).

The Disaster Management Center of Sri Lanka and the United Nations Development Program (UNDP) recorded twenty-two tropical cyclones which impacted Sri Lanka during 1881–2001 (Srisangeerthanan et al., 2015). Besides, seventeen cyclones such as Ward, Nisha, Nilam, Viyaru, Madi, Nada and Roanu had impacted the east coast of Sri Lanka from 2000 to 2018 (Srisangeerthanan et al.,

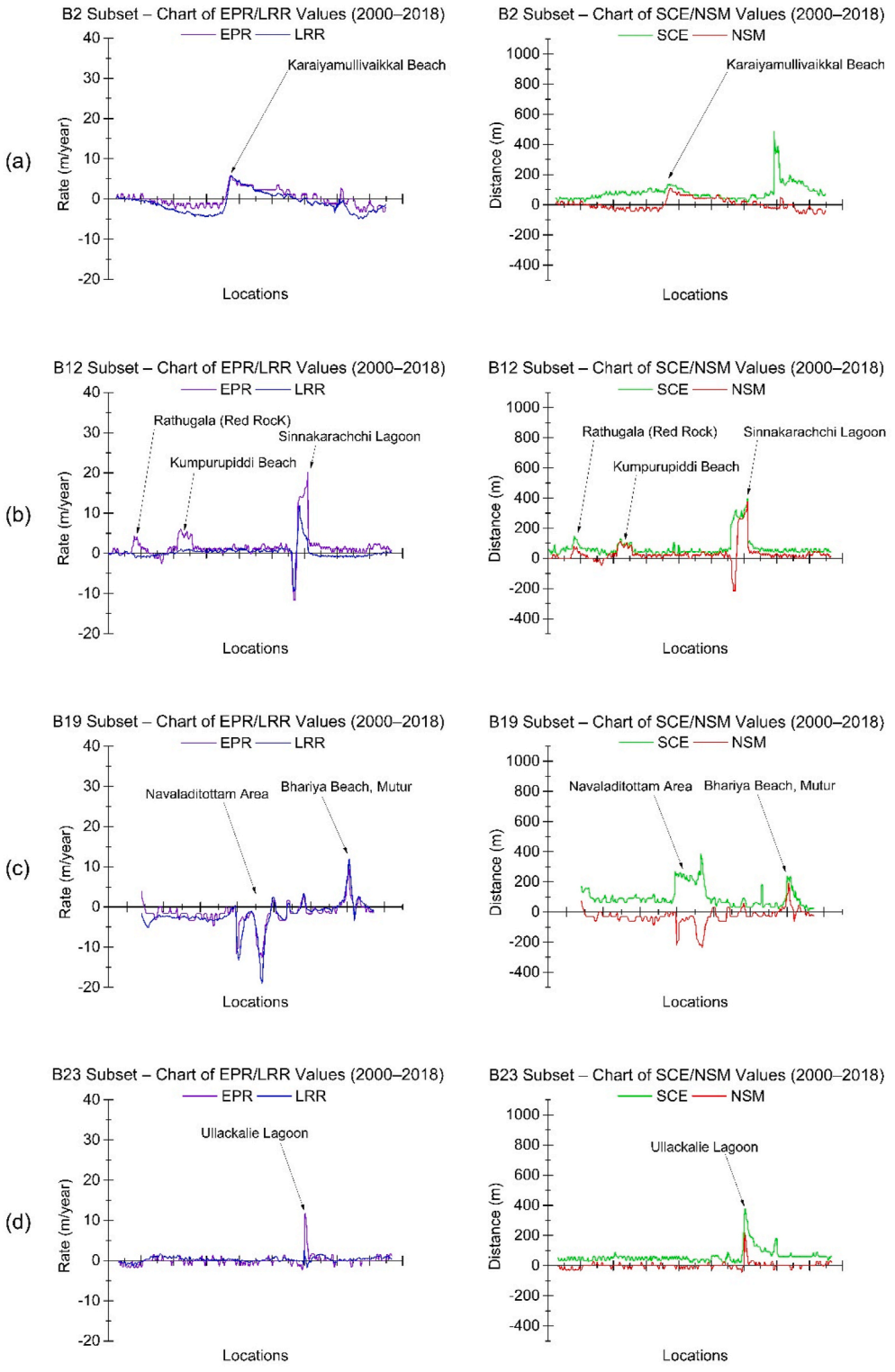

Fig. 8. DSAS statistical graphs in (a) B2, (b) B12, (c) B19, and (d) B23 subsets.

2015; Uddin et al., 2019). For example, Kyant and Nada cyclones occurred on 21–28 October and 29 November–2 December in 2016, respectively (Xu et al., 2020). Satellite images show that the Batticaloa Barmouth area is subjected to significant landform changes (i.e. accretion) during the inter-monsoon period (Fig. 10b). The east coast of Sri Lanka is experienced high-energy oceanic waves during the

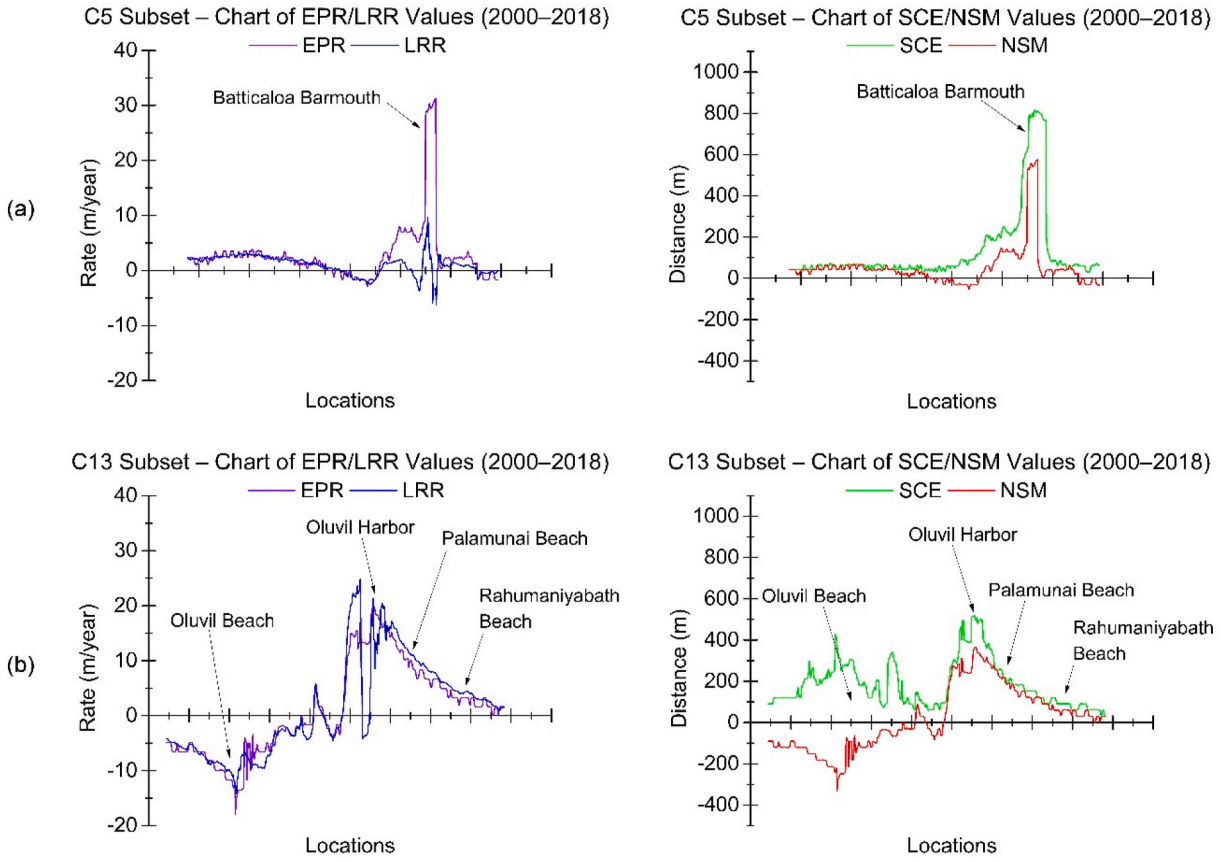

Fig. 9. DSAS statistical graphs in (a) C5, and (b) C13 subsets.

northeast monsoon (from December to February), whereas low-energy waves are observed during inter-monsoon periods of March to April and October to November (Amalan et al., 2018). Consequently, the cyclones created random oceanic currents and destructive oceanic waves. These cyclones can be identified as possible drivers for short-term landform changes along the east coast of Sri Lanka. Similarly, Satyanarayana et al. (2017) also identified that these types of destructive oceanic waves altered coastal geomorphology along the east coast of Sri Lanka.

Most construction firms are limited by the political and social instability of the study area. However, rapid industrialization and urbanization had witnessed a great rise since the end of the civil war in 2009. For example, coastal engineering projects such as harbors, and coastal infrastructures (e.g. groins and breakwaters) have been constructed along the east coast of Sri Lanka. Groins and breakwaters change longshore and cross-shore current patterns, respectively (Ratnayake et al., 2018; Senevirathna et al., 2018). For example, satellite images show that Oluvil Harbor altered the counterclockwise longshore sediment transportation (Fig. 6e and 10c). In this case, the southern part of the harbor and Palamunai beach are subjected to sediment accretion and the northern part of the harbor is subjected to severe coastal erosion due to an imbalance of nearshore sediment dynamics (Figs. 6e, 10c and 11c). Therefore, man-made activities can also be identified as a possible driver to control the short-term sediment budgets along the east coast of Sri Lanka.

Several studies have been investigated past sea-level changes (e.g. middle Holocene sea-level highstands) along the south and southwest coasts of Sri Lanka (Ratnayake et al., 2017; Mann et al., 2019; Yokoyama et al., 2019). The continental shelf of the south and southwest coasts is narrow and has the steepest continental slope in the world (de Vos et al., 2014), and the south and southwest coasts are thus vulnerable to climate-induced sea-level rising. However, the continental shelf of the east coast is wide and merges with the platform of India in its northern part (Ratnayake, 2016). According to Palamakumbure et al. (2020), the sea-level has increased at a rate of 0.288 ± 0.118 in Sri Lanka. Consequently, these factors suggest that climate-induced sea-level changes have less influence on rapid (from 2000 to 2018) and detectable landform changes on the east coast of Sri Lanka, using remote sensing and GIS techniques.

Fig. 10. QuickBird satellite images show erosional or accretion anomalies in (a) C23, (b) C5, and (c) C13 subsets.

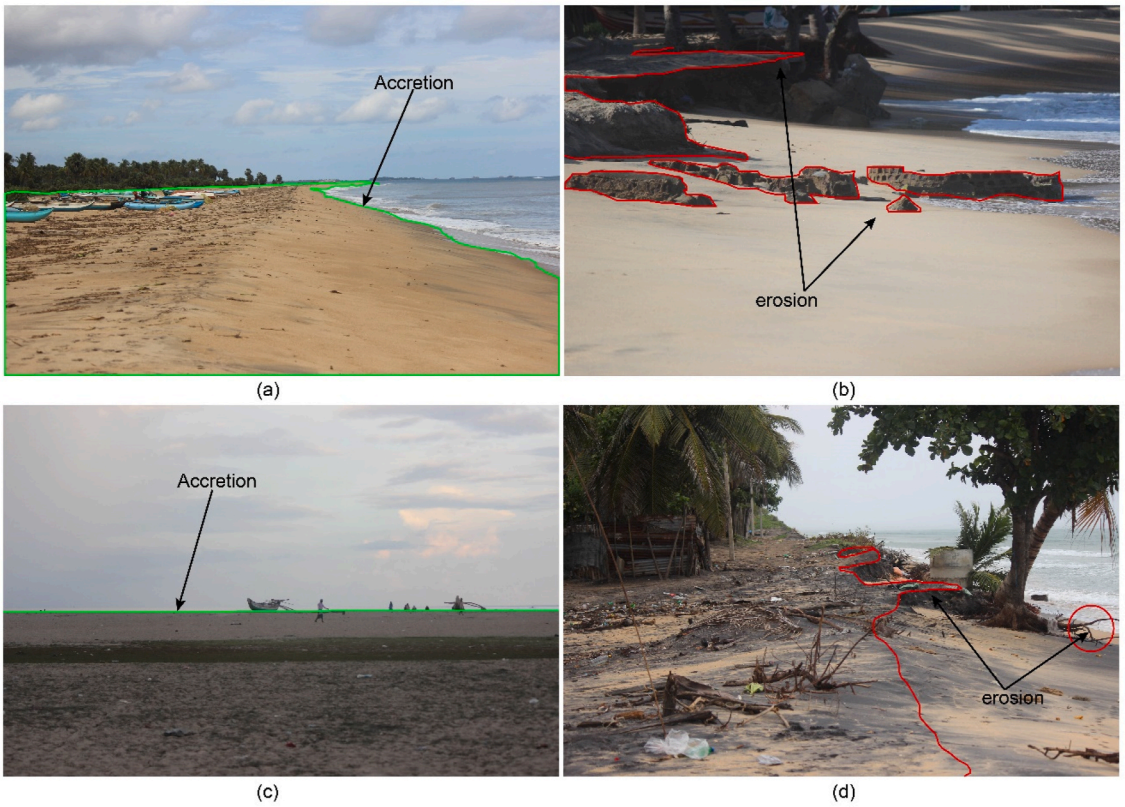

Fig. 11. Field photographs at (a) Verugal, (b) Thirukkovil, (c) Palamunai, and (d) Kokkilai black sand beaches along the east coast of Sri Lanka.

5. Conclusions

The shoreline analysis system gained meaningful information about shoreline changes on the eastern coast of Sri Lanka (See appendix 4 video). The short-term shoreline changes (i.e. either accretion or erosion) occur due to both natural and anthropogenic processes. However, climate-induced sea-level rising can be identified as a centurial to millennium scale driver for landform changes along this coast. In general, the upper part of the east coast is exposed to coastal accretion, and the lower part of the east coast is exposed to coastal erosion. Nevertheless, the coastal accretion or erosion along the east coast of Sri Lanka is site-specific. In addition, the rapid shoreline changes can be identified due to anthropogenic activities such as sand mining and coastal engineering projects (e.g. Oluvil harbor). The outcome of this study can be applied to sustainable coastal zone management, and to design the proper coastal engineering structures along the east coast of Sri Lanka.

Author statement

W.A.D.B. Weerasingha: analysis & interpretation, writing & editing, Amila Sandaruwan Ratnayake: interpretation, writing & editing, supervision, funding acquisition.

Ethical statement

On behalf of all authors, I declare that all ethical practices have been followed in relation to the development, writing, and publication of the article.

Declaration of competing interest

The authors declare that they have no known competing financial interests or personal relationships that could have appeared to influence the work reported in this paper.

Acknowledgments

The authors would like to acknowledge the financial assistance for this study by an Accelerating Higher Education Expansion and Development (AHEAD) Development Oriented Research (DOR) grant funded by the World Bank.

Appendix A. Supplementary data

Supplementary data to this article can be found online at https://doi.org/10.1016/j.rsase.2022.100763.

References

Acharya, T., Lee, D., Yang, I., Lee, J., 2016. Identification of water bodies in a Landsat 8 OLI image using a J48 decision tree. Sensors 16, 1075. https://doi.org/10.3390/s16071075.

Acharya, T., Subedi, A., Yang, I., Lee, D., 2018. Combining water indices for water and background threshold in Landsat image. Proceedings 2, 143. https://doi.org/10.3390/ecsa-4-04902.

Adikaram, M., Pitawala, A., Ishiga, H., Jayawardana, D., Eichler, C.M., 2021. An ecological risk assessment of sediments in a developing environment-Batticaloa lagoon, Sri Lanka. J. Mar. Sci. Eng. 9, 73. https://doi.org/10.3390/jmse9010073.

Amalan, K., Ratnayake, A.S., Ratnayake, N.P., Weththasinghe, S.M., Dushyantha, N., Lakmali, N., Premasiri, R., 2018. Influence of nearshore sediment dynamics on the distribution of heavy mineral placer deposits in Sri Lanka. Environ. Earth Sci. 77, 737. https://doi.org/10.1007/s12665-018-7914-4.

Arjasakusuma, S., Kusuma, S.S., Saringatin, S., Wicaksono, P., Mutaqin, B.W., Rafif, R., 2021. Shoreline dynamics in East Java Province, Indonesia, from 2000 to 2019 using multi-sensor remote sensing data. Land 10, 100. https://doi.org/10.3390/land10020100.

Asmadin, S.V., Sofian, I., Jaya, I., Wijanarto, A., 2018. Feature extraction of coastal surface inundation via water index algorithms using multispectral satellite on North Jakarta. IOP Conf. Ser. Earth Environ. Sci. 176, 012032 https://doi.org/10.1088/1755-1315/176/1/012032.

de Vos, A., Pattiaratchi, C.B., Wijeratne, E.M.S., 2014. Surface circulation and upwelling patterns around Sri Lanka. Biogeosciences 11, 5909–5930. https://doi.org/10.5194/bg-11-5909-2014.

Desprats, J.F., Garcin, M., Attanayake, N., Pedreros, R., Siriwardana, C., Fontaine, M., De Silva, U., 2010. A 'coastal-hazard GIS' for Sri Lanka. J. Coast Conserv. 14, 21–31. https://doi.org/10.1007/s11852-009-0084-5.

Duong, T.M., Ranasinghe, R., Callaghan, D.P., 2021. Probabilistic projections of the stability of small tidal inlets at century time scale using a reduced complexity approach. Sci. Rep. 11, 1–14. https://doi.org/10.1038/s41598-021-01945-5.

Foga, S., Scaramuzza, P., Guo, S., Zhu, Z., Dilley, R., Beckmann, T., Schmidt, G., Dwyer, J., Hughes, J.M., Laue, B., 2017. Cloud detection algorithm comparison and validation for operational Landsat data products. Remote Sens. Environ. 194, 379–390. https://doi.org/10.1016/j.rse.2017.03.026.

Gunasinghe, G.P., Ruhunage, L., Ratnayake, N.P., Ratnayake, A.S., Samaradivakara, G.V.I., Jayaratne, R., 2021. Influence of manmade effects on geomorphology, bathymetry and coastal dynamics in a monsoon-affected river outlet in Southwest coast of Sri Lanka. Environ. Earth Sci. 80, 1–16. https://doi.org/10.1007/s12665-021-09555-0.

Himmelstoss, E.A., Henderson, R.E., Kratzmann, M.G., Farris, A.S., 2018. Digital Shoreline Analysis System (DSAS) Version 5.0 User Guide (No. 2018-1179). US Geological Survey. https://doi.org/10.3133/ofr20181179.

Islam, M.M., Rahman, M.S., Kabir, M.A., Islam, M.N., Chowdhury, R.M., 2020. Predictive assessment on landscape and coastal erosion of Bangladesh using geospatial techniques. Remote Sens. Appl.: Soc. Environ. 17, 100277 https://doi.org/10.1016/j.rsase.2019.100277.

Lowry, K., Wickremeratne, H.J.M., 1988. Coastal area management in Sri Lanka. Ocean Yearbk. 7, 263–293. https://doi.org/10.1163/221160088X00174.

Malahlela, O.E., 2016. Inland waterbody mapping: towards improving discrimination and extraction of inland surface water features. Int. J. Rem. Sens. 37, 4574–4589. https://doi.org/10.1080/01431161.2016.1217441.

Mann, T., Bender, M., Lorscheid, T., Stocchi, P., Vacchi, M., Switzer, A.D., Rovere, A., 2019. Holocene sea levels in southeast Asia, Maldives, India and Sri Lanka: the SEAMIS database. Quat. Sci. Rev. 219, 112–125. https://doi.org/10.1016/j.quascirev.2019.07.007.

Masek, J., Vermote, E., Saleous, N., Wolfe, R., Hall, F., Huemmrich, K., Gao, F., Kutler, J., Lim, T., 2006. A Landsat surface reflectance dataset for North America, 1990–2000. Geosci. Rem. Sens. Lett. IEEE 3, 68–72. https://doi.org/10.1109/LGRS.2005.857030.

Palamakumbure, L., Ratnayake, A.S., Premasiri, H.M.R., Ratnayake, N.P., Katupotha, J., Dushyantha, N., Weththasinghe, S., Weerakoon, W.A.P., 2020. Sea-level inundation and risk assessment along the south and southwest coasts of Sri Lanka. Geoenvironmental Disasters 7, 17. https://doi.org/10.1186/s40677-020-00154-y.

Quang, D.N., Ngan, V.H., Tam, H.S., Viet, N.T., Tinh, N.X., Tanaka, H., 2021. Long-term shoreline evolution using DSAS technique: a case study of Quang Nam Province, Vietnam. J. Mar. Sci. Eng. 9, 1124. https://doi.org/10.3390/jmse9101124.

Ratnayakage, S.M.S., Sasaki, J., Suzuki, T., Jayaratne, R., Ranawaka, R.A.S., Pathmasiri, S.D., 2020. On the status and mechanisms of coastal erosion in Marawila Beach, Sri Lanka. Nat. Hazards 103, 1261–1289. https://doi.org/10.1007/s11069-020-04034-4.

Ratnayake, A.S., 2016. Evolution of coastal landforms during the Holocene Epoch along the west and southeast coasts of Sri Lanka. Interdiscipl. Environ. Rev. 17, 60–69.

Ratnayake, A.S., Sampei, Y., Ratnayake, N.P., Roser, B.P., 2017. Middle to late Holocene environmental changes in the depositional system of the tropical brackish Bolgoda Lake, coastal southwest Sri Lanka. Palaeogeogr. Palaeoclimatol. Palaeoecol. 465, 122–137. https://doi.org/10.1016/j.palaeo.2016.10.024.

Ratnayake, N.P., Ratnayake, A.S., Azoor, R.M., Weththasinghe, S.M., Seneviratne, I.D.J., Senarathne, N., Premasiri, R., Dushyantha, N., 2019. Erosion processes driven by monsoon events after a beach nourishment and breakwater construction at Uswetakeiyawa beach, Sri Lanka. SN Appl. Sci. 1, 52. https://doi.org/10.1007/s42452-018-0050-7.

Ratnayake, N.P., Ratnayake, A.S., Keegle, P.V., Mallawa Arachchi, M.A.K.M., Premasiri, H.M.R., 2018. An analysis of beach profile changes subsequent to the Colombo Harbor Expansion Project, Sri Lanka. Environ. Earth Sci. 77, 24. https://doi.org/10.1007/s12665-018-7234-8.

Satyanarayana, B., van der Stocken, T., Rans, G., Kodikara, K.A.S., Ronsmans, G., Jayatissa, L.P., Husain, M.L., Koedam, N., Dahdouh-Guebas, F., 2017. Island-wide coastal vulnerability assessment of Sri Lanka reveals that sand dunes, planted trees and natural vegetation may play a role as potential barriers against ocean surges. Global Ecol. Conservat. 12, 144–157. https://doi.org/10.1016/j.gecco.2017.10.001.

Senevirathna, E., Edirisooriya, K., Uluwaduge, S., Wijerathna, K., 2018. Analysis of causes and effects of coastal erosion and environmental degradation in southern coastal belt of Sri Lanka special reference to Unawatuna coastal area. Procedia Eng. 212, 1010–1017. https://doi.org/10.1016/j.proeng.2018.01.130.

Srisangeerthanan, S., Lewangamage, C.S., Wickramasuriya, S.S., 2015. Tropical Cyclone Damages in Sri Lanka, 40. Wind Engineers JAWE, pp. 294–302. https://doi.org/10.5359/jawe.40.294.

Subasinghe, H.C.S., Ratnayake, A.S., Sameera, K.A.G., 2021. State-of-the-art and perspectives in the heavy mineral industry of Sri Lanka. Mineral Econ. 34, 427–439. https://doi.org/10.1007/s13563-021-00274-3.

Thomas, J., Kumar, S., Sudheer, K.P., 2020. Channel stability assessment in the lower reaches of the Krishna River (India) using multi-temporal satellite data during 1973–2015. Remote Sens. Appl.: Soc. Environ. 17, 100274 https://doi.org/10.1016/j.rsase.2019.100274.

Uddin, M.J., Li, Y., Cheung, K.K., Nasrin, Z.M., Wang, H., Wang, L., Gao, Z., 2019. Rainfall contribution of tropical cyclones in the Bay of Bengal between 1998 and 2016 using TRMM satellite data. Atmosphere 10, 699. https://doi.org/10.3390/atmos10110699.

Vermote, E., Justice, C., Claverie, M., Franch, B., 2016. Preliminary analysis of the performance of the Landsat 8/OLI land surface reflectance product. Remote Sens. Environ. 185, 46–56. https://doi.org/10.1016/j.rse.2016.04.008.

Wijeratne, S., 2016. Geomorphological changes caused by tsunami 2004 in the coastal environment of Weligama Bay in Southern Sri Lanka. Sri Lanka J. Soc. Sci. 38, 117. https://doi.org/10.4038/sljss.v38i2.7395.

Wijetunge, J.J., 2009. Field measurements and numerical simulations of the 2004 tsunami impact on the East Coast of Sri Lanka. Pure Appl. Geophys. 166, 593–622. https://doi.org/10.1007/s00024-009-0458-5.

Xu, H., 2006. Modification of normalized difference water index (NDWI) to enhance open water features in remotely sensed imagery. Int. J. Rem. Sens. 27, 3025–3033. https://doi.org/10.1080/01431160600589179.

Xu, H., Yu, R., Tang, D., Liu, Y., Wang, S., Fu, D., 2020. Effects of tropical cyclones on sea surface salinity in the Bay of Bengal based on SMAP and Argo data. Water 12, 2975. https://doi.org/10.3390/w12112975.

Yan, D., Huang, C., Ma, N., Zhang, Y., 2020. Improved Landsat-based water and snow indices for extracting lake and snow cover/glacier in the Tibetan Plateau. Water 12, 1339. https://doi.org/10.3390/w12051339.

Yokoyama, Y., Hirabayashi, S., Goto, K., Okuno, J.I., Sproson, A.D., Haraguchi, T., Miyairi, Y., 2019. Holocene Indian Ocean sea level, Antarctic melting history and past Tsunami deposits inferred using sea level reconstructions from the Sri Lankan, Southeastern Indian and Maldivian coasts. Quat. Sci. Rev. 206, 150–161. https://doi.org/10.1016/j.quascirev.2018.11.024.